

Hybrid Solar Absorber–Emitter by Coherence-Enhanced Absorption for Improved Solar Thermophotovoltaic Conversion

Yang Wang, Lin Zhou,* Ye Zhang, Jianyu Yu, Baili Huang, Yuxi Wang, Yun Lai, Shining Zhu, and Jia Zhu*

Spectrum selective absorbers and emitters, with advantages of high temperature tolerance, wide angle insensitivity, and scalable fabrication processes, are crucial components for solar thermophotovoltaics (STPV). A bifunctional hybrid absorber–emitter (HAE) for efficient STPV by sequentially depositing $\text{HfO}_2/\text{Mo}/\text{HfO}_2$ films on a metallic surface is demonstrated here. Simultaneous broadband solar absorption and narrowband infrared emission are enabled by the same surface of the structure. By fine steering coherent perfect absorption of the ultrathin Mo film and destructive interference of interfacial reflections across the top HfO_2 layer, the HAE exhibits a measured emissivity of 0.97 at $1.8\ \mu\text{m}$ as well as an average absorptivity of $\approx 80\%$ over 400–1000 nm, respectively, both of which are well maintained under nearly omnidirectional irradiance ($\approx 80^\circ$) and up to 1373 K thermal stability test. The features of multiple coherence-enhanced all-in-one single-surface HAE (dual-spectrum selectivity, wide angle tolerance, high temperature stability, etc.), make the HAE a good candidate for specialized efficient STPV. As a demonstration, it is theoretically shown that the HAE-based cage-type STPV can enable a maximal system efficiency increment of $>15\%$ compared to the double-side planar systems, providing a potential route leading to integrated STPV–TPV systems for all-climate operation in future.

Spectrally selective absorbers and emitters are key components in various energy conversion applications such as solar thermophotovoltaics (STPV),^[1–3] radiative cooling,^[4,5] solar steam generation,^[6–8]

etc. In order to maximize the utilization of solar energy, STPV requires the cooperative spectral manipulation of a broadband solar absorber and a narrowband infrared emitter. An ideal STPV absorber must simultaneously absorb input power and suppress radiation loss, while an STPV emitter should possess high emissivity only at the target infrared wavelength matching well with the base PV cell.^[9] Extensive efforts have been devoted to design and fabricate such absorbers and emitters, including intrinsically spectrally selective materials,^[10–12] multilayer structures,^[13–17] cermetes,^[18] plasmonic metamaterials,^[19–26] and photonic crystals.^[27–31] Up to now, most of the reported absorbers and emitters are demonstrated by two isolated structures,^[1,2] such as the compound metallic structures patterned on both sides of a substrate in a recently developed STPV system.^[30] Such an optical design is intuitive and straightforward. However, the double-side lithography process severely increases the fabrication and systematic complexity. A hybrid absorber–emitter (HAE) with the


two functions built on the same surface of the structure is beneficial for STPV. Great efforts have been made to integrate these two functionalities of broadband-absorption and narrowband-emission into one metasurface or plasmonic structure.^[32–34] However, these structures are rather complicated and the well-defined morphologies are unstable at high temperature that the STPV system requires. An integrated HAE with ideal spectral selectivity, high temperature tolerance as well as scalable fabrication process is highly pursued but still elusive.

Most specifically, in this work, we present a much simpler HAE design of a layered structure on a metallic surface based on multiple coherence-enhanced absorption, especially the coherent perfect absorption (CPA) effect. Such a structure is lithography-free, scalable, and possesses excellent thermal stability. In addition, the full spectrum responses demonstrate weak angular-dependence and polarization sensitivity, all of which make it beneficial for the STPV applications.

The CPA phenomenon was first proposed for the case that two coherent counter-propagating light beams can be totally absorbed in a dielectric Fabry–Pérot cavity,^[35–37] which was

Y. Wang, Prof. L. Zhou, Y. Zhang, J. Yu, Y. Wang, Prof. Y. Lai, Prof. S. Zhu, Prof. J. Zhu
National Laboratory of Solid State Microstructures
College of Engineering and Applied Sciences
School of Physics
Key Laboratory of Intelligent Optical Sensing and Manipulation
Ministry of Education
Nanjing University
Nanjing 210093, P. R. China
E-mail: linzhou@nju.edu.cn; jiazhu@nju.edu.cn

Prof. L. Zhou, B. Huang
Department of Chemistry
Columbia University
New York, NY 10027, USA

 The ORCID identification number(s) for the author(s) of this article can be found under <https://doi.org/10.1002/adom.201800813>.

DOI: 10.1002/adom.201800813

then transferred to the case of single beam illumination in an ultrathin film based on reflectors.^[38–45] In an ideal thin film-based CPA structure, the film thickness d_m is much thinner than the wavelength and thus $kd_m \ll 1$ (k is the wave vector). Also, because either the tangential electric or magnetic field is almost constant across the film, we have

$$1 + r_{E(H)} \approx t_{E(H)}, \quad (1)$$

where $r_{E(H)}$ and $t_{E(H)}$ are the reflection and transmission coefficient of the film, respectively. If only one of them is constant, absorption happens with a maximal value of 50% since $-r_{E(H)} \approx t_{E(H)} \approx 0.5$. By introducing a reflector, a perfect absorption of 100% efficiency is feasible when the thin film structure enables destructive interference at the interface and the dielectric constant (ϵ) of the ultrathin film satisfies the following equation at normal incidence:

$$\epsilon = i \frac{2}{kd_m (\eta_E^{-1} e^{-i\phi} + 1)}, \quad (2)$$

where η_E and ϕ are reflection amplitude and phase shift of the reflector, respectively.^[38]

Our integrated bifunctional HAE, a planar $\text{HfO}_2/\text{Mo}/\text{HfO}_2$ layered structure on the surface of a refractory metal substrate, is schematically shown in **Figure 1a**. To enable pronounced thermal stability for STPV, all the employed materials are of high temperature melting points. Specifically, compared to other refractory metals such as tungsten and tantalum, molybdenum of lower melting temperature is more favorable

for the experimental realization of ultrathin smooth layer. The infrared absorption is designed by single-beam CPA structure. Both the inner HfO_2 layer and the substrate serve as phase delay reflectors so that the incident and reflected light are strongly absorbed in the ultrathin metal film. The top HfO_2 layer provides the reflection manipulation in visible via destructive interference between different interfacial reflection beams and thus results in efficient light absorption in solar spectrum. The two coherence-enhanced absorption effects form the basis of the ideal bifunctional HAE design of selective narrowband infrared emission for PV cell of STPV as well as broadband solar absorption, respectively, as shown in **Figure 1b**.

First of all, we numerically demonstrate the HAE design of appealing absorption performance in the visible and infrared wavelength ranges. **Figure 2a** shows the calculated absorption spectra of three typical HAE structures with the same CPA layer of 5 nm thick Mo, in which $d_1 = 200$ nm and $d_2 = 50$ nm for Design I (solid black line), $d_1 = 300$ nm and $d_2 = 65$ nm for Design II (dashed red line), as well as $d_1 = 400$ nm and $d_2 = 70$ nm for Design III (dotted blue line), respectively. Here d_1 and d_2 refer to the inner and outer HfO_2 layers, respectively (see **Figure 1a**). It is clear that the infrared emission peak can be flexibly tuned by changing the thickness of the inner HfO_2 layer d_1 , in good agreement with Equation (2). The quantitative dependence of the emission peak wavelength on d_1 is further shown in **Figure 2b**. We also calculate the normalized electric and magnetic field of Design I at 1470 nm. The diagram shows a typical thin film CPA feature (**Figure 2c**) that the electric field is almost constant in amplitude while magnetic field is drastically decreasing across the ultrathin Mo layer. Note that the electric field is quite approaching to that of free space electromagnetic field, verifying that there is almost no reflection and thus perfect absorption is achieved.

Wide angle optical absorption/emission is highly desired in most energy conversion systems, especially in the thermal emitter of STPV. Beneficial from the unique property of CPA-dominated angular insensitive spectrum response,^[39] the infrared emission peak at 1470 nm of our HAE exhibits a distinct angular independent feature up to 80° , as demonstrated in the angular-resolved absorption spectra in **Figure 2d** (calculated by transfer matrix method, for both transverse electric (TE) and transverse magnetic (TM) modes). Apart from the angular-independent infrared peak, pronounced visible absorption peaks are achieved simultaneously due to the destructive interfacial interference, beneficial for the broadband solar harvesting requirement. Although it is not as perfect as the CPA peak in angular dependency, these visible peaks remain almost unchanged in wavelength with merely slight decrease in intensity for $>60^\circ$ illumination.

We then experimentally verified the coherence-enhanced optical design of HAE with three samples prepared (referred to the three designs in **Figure 2a**, respectively). In the experiment, we fabricated the planar HAE structures by sequentially depositing a HfO_2 film (d_1) and ultrathin molybdenum (Mo) film on an Mo substrate, followed by a second HfO_2 film (thickness d_2) as the top layer. The radio frequency magnetron sputtering was conducted in Argon gas of 0.29 Pa at room temperature. The cross sectional scanning electron microscope (SEM) image of the fabricated sample is obtained using

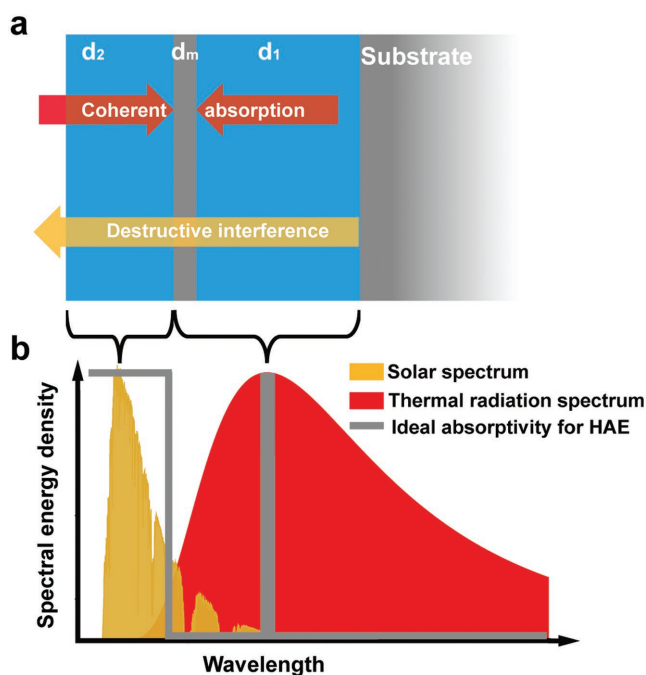


Figure 1. The schematic optical design of the bifunctional HAE. a) Layered structure with two coherence-enhanced effects: coherent perfect absorption (red arrow) as well as destructive interference (yellow arrow). b) Ideal spectral selectivity of the HAE: step-functional solar absorption as well as narrowband infrared emission peak.

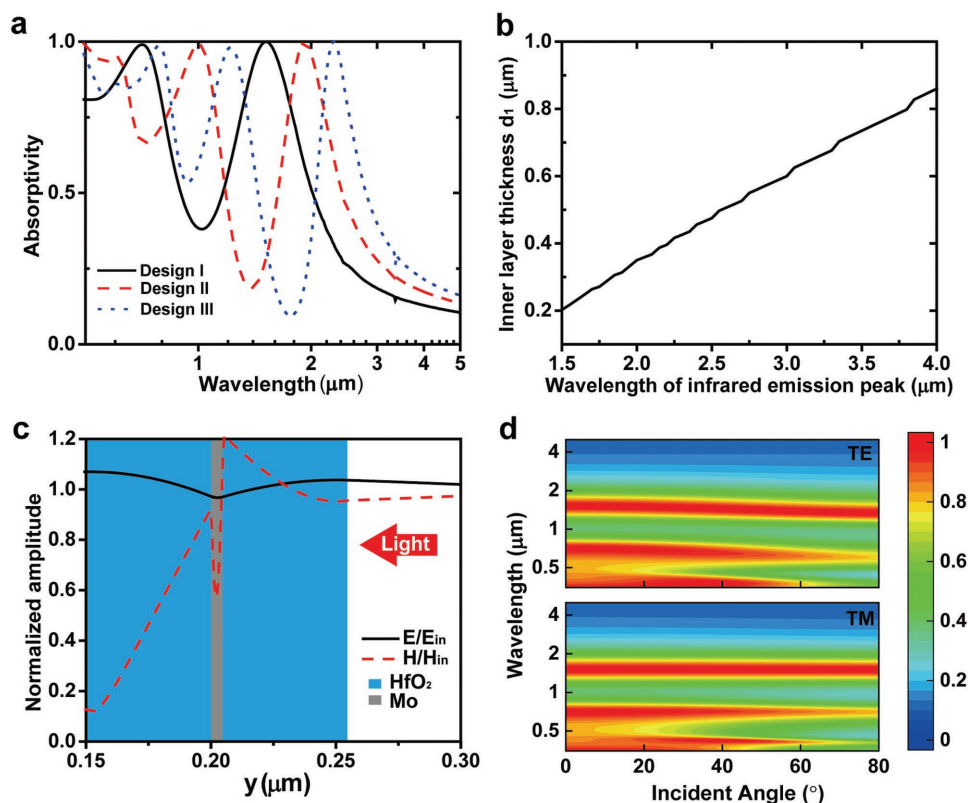


Figure 2. Calculated absorption performance of the HAE. a) Absorptivity of three typical HAE designs. All the designs are based on a 5 nm thick Mo layer sandwiched with inner and outer HfO_2 films of different thicknesses (d_1, d_2): (200, 50 nm) for Design I (black solid line), (300, 60 nm) for Design II (red dashed line), (400, 70 nm) for Design III (blue dotted line), respectively. b) Required thickness d_1 of the inner HfO_2 layer for different target infrared emission peaks. c) The normalized electric and magnetic field profiles of $\lambda = 1470$ nm of Design I. d) Angular dependence of absorptivity of Design I for TE (upper) and TM (lower) modes calculated by the transfer matrix method, respectively.

a high resolution focus ion beam etching method, and photographed at a 52° angle (Figure 3a). The ultrathin Mo layer sandwiched between two HfO_2 layers can be easily observed. The distinct black appearance (inset of Figure 3a) indicates the efficient absorption for visible light. The measured absorptivity from visible to mid-infrared wavelength of the three samples (noted as I, II, and III, respectively) demonstrate the dual functions of an absorber and emitter via the same surface (Figure 3b). As expected, the measured emission peak experiences red-shifts as the thickness of inner HfO_2 layer increases, achieving a maximal emissivity of 97% at $1.8 \mu\text{m}$ in sample I. The absorptivity spectra at different incident angles in the visible and infrared ranges are measured as well (Figure 3c,d), revealing excellent wide-angle tolerance up to 50° . The multiple absorption peaks in the visible range show good overlap with the solar spectral irradiance, beneficial for the broadband solar harvesting simultaneously (the average absorptivity reaches $\approx 80\%$).

Apart from the wide-angle spectral selectivity, the high-temperature performance of our HAE is advantageous as well. The temperature-dependent absorptivity spectra were measured by conducting an in situ thermal heating experiment combined with microscopic infrared spectroscopy (Linkam THMS600, Bruke vertex 70), as shown in Figure 3e. Except for finite self-radiation after $2 \mu\text{m}$, the measured spectra are stable across the

measured wavelength range as the sample temperature raises from room temperature to 873 K (the upper limit of temperature available in our lab). To further demonstrate the high-temperature stability, especially in the vacuum environment (as operated in the real STPV system), we conducted annealing experiments at 1173 and 1373 K under 0.2 Pa, during which the sample is heated from room temperature to target temperature in 1 h, and held there for 30 min, and then cooled down naturally. As shown in Figure 3f, the absorptivity spectra measured before and after the in-vacuum annealing processes agree well with each other up to 1373 K (see Figure S1 in the Supporting Information for even higher temperature annealing results up to 1473 K). It is worth noting that the thermal heating process causes most materials to expand and can even induce changes in their dielectric constants; both of these changes will in turn affect their optical performance. Fortunately, the two materials employed in our HAE (HfO_2 and Mo) have similar expansion coefficients ($5.8 \times 10^{-6} \text{ }^\circ\text{C}^{-1}$ for HfO_2 , $5.35 \times 10^{-6} \text{ }^\circ\text{C}^{-1}$ for Mo at room temperature,^[46,47] respectively) and relatively stable dielectric constants. These characteristics make it possible to maintain a stable absorption spectrum in spite of elevated temperatures.

As a systematic demonstration, we show that our CPA-based HAE structure can be an ideal choice for specialized STPV systems thanks to its capability of suppressed radiation loss, which is responsible for 30–40% of an object heat loss.^[30]

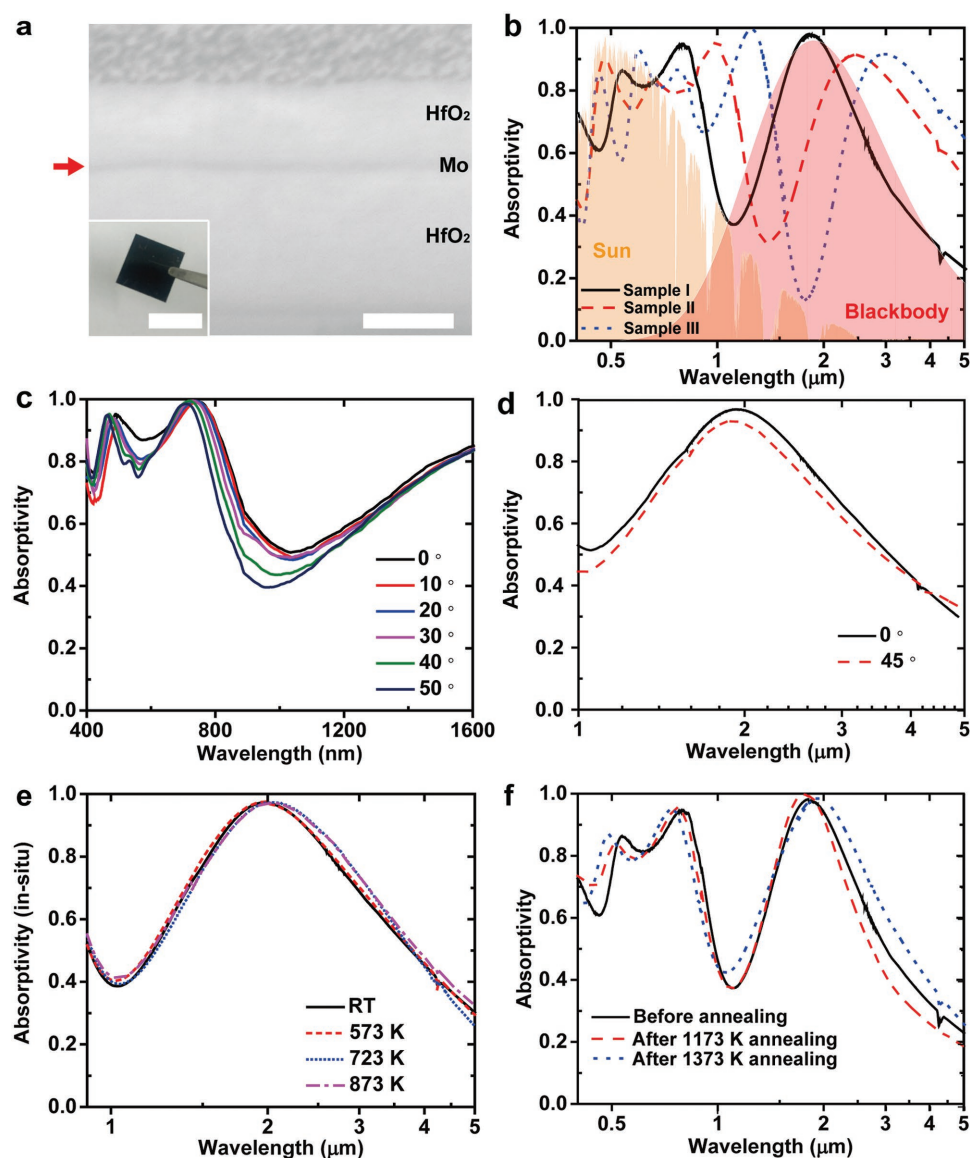


Figure 3. Measured absorptivity spectra of the HAE. a) Cross-sectional SEM image of sample I with a 200 nm Pt protection layer on top from Ga ion irradiance (scale bar: 100 nm). Red arrow indicates the 5 nm Mo layer. Inset is the optical image (scale bar: 10 mm). b) Absorptivity of sample I, II, and III with emission peak of 1.8, 2.4, and 3 μm , respectively. The orange and red areas indicate the solar spectrum and blackbody radiation spectrum at 1550 K, respectively. c,d) Angular dependence of sample I in (c) visible and (d) infrared range. e) In situ absorptivity of sample I from room temperature to 873 K. f) Absorptivity spectra of sample I measured before and after the in-vacuum annealing tests under 1173 and 1373 K, respectively.

Taking the cage-type STPV for example, the HAE possesses unique advantages of the one-side structure and efficient trapping capability of thermal radiation compared with most of the conventional STPV strategies of double-side structures, such as controlling the area ratio between the absorber and the emitter.^[2,48] Figure 4a shows the schematic system of the HAE-based cage-type STPV with the PV cell curved within a small aperture. The HAE device absorbs the solar irradiance through the narrow aperture of the cell cage, and transfers the captured broadband irradiance into a narrowband thermal emission, which finally directionally irradiates toward the surrounding PV cells, nearly covering the 4π solid angle. The absorbed photons

can hardly escape out of the cage-type STPV because of the low leaking probability through the narrow aperture, ensuring a high system efficiency.

Note that the radiation-loss efficiency (η_r) is determined by the system structure, which is nearly zero in the cage-type STPV but greatly increased with the absorber area in a planar STPV. Without loss of generality, a conventional planar STPV system involves a double-side isolated emitter and an absorber with a large area ratio of 10:1 is considered. One may find in Figure 4b that, even for planar STPV with large area ratio, the estimated system efficiency loss due to thermal emission will overpass 15%.

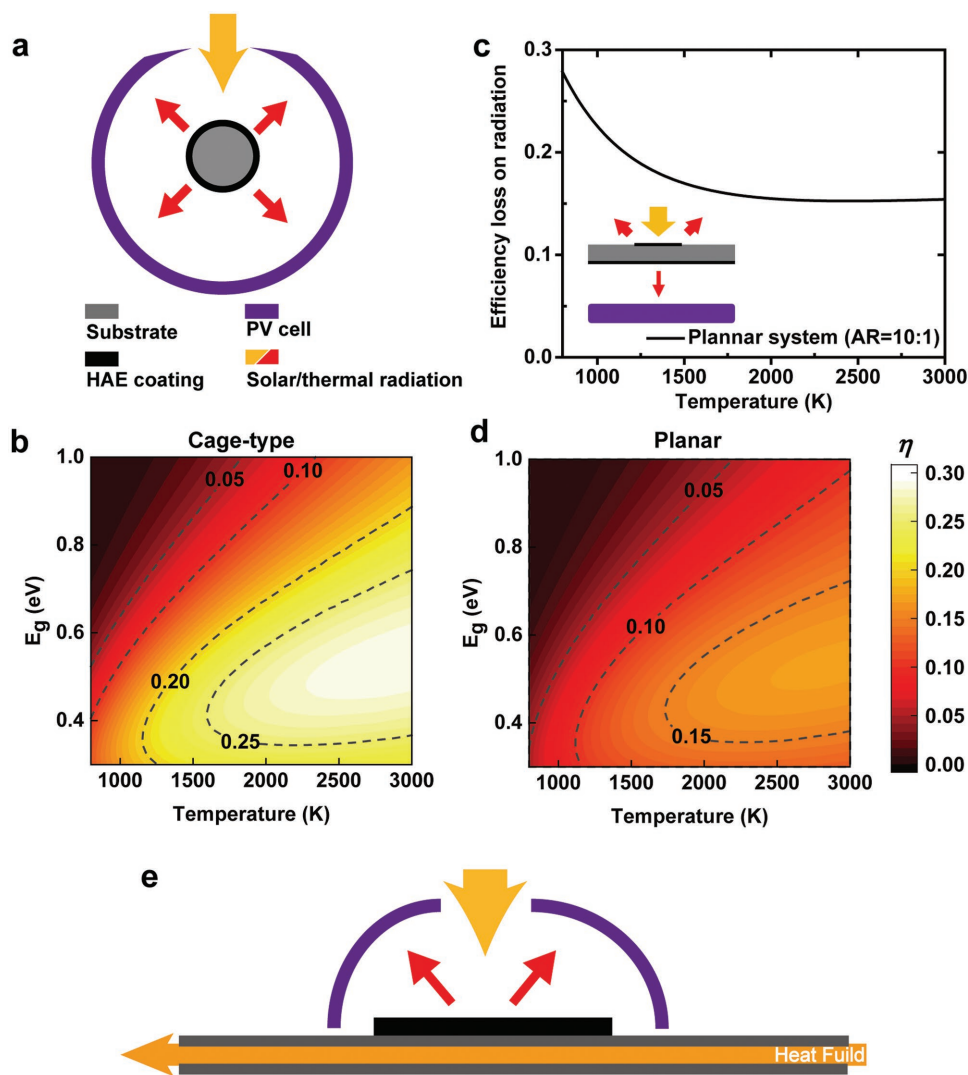


Figure 4. Calculated system performance of STPV system. a) Schematic of cage-type STPV system. b) Radiative heat loss in a planar STPV system. Inset: schematic. c) System efficiency of cage-type STPV. d) System efficiency of planar STPV. e) Schematic of an all-climate STPV-TPV system.

The overall system efficiency (η) of STPV is determined by the absorption efficiency η_a , radiation-loss efficiency η_r , and solar cell efficiency η_c , which is expressed as

$$\eta = (\eta_a - \eta_r)\eta_c \quad (3)$$

Direct comparisons of calculated system efficiency of the HAE-based cage-type and planar STPVs are depicted in Figure 4c,d. Because of the unique radiation suppression, our HAE-based cage-type STPV can enable a system efficiency promotion of >15% compared to planar STPV (see detailed calculations in Part II, Supporting Information). In addition, thanks to the narrowband emission, our HAE-based STPV can earn 10% efficiency increment compared to the counterpart of broadband emitters (Part III, Supporting Information). Note that in a real system, the unavoidable conduction loss through the absorber/emitter's holder and the nonideal view factor of emitter^[49] would introduce extra heat loss, leading to the

currently low system efficiency of no more than 10%.^[1–3,48] Our HAE-based cage-type STPV system can provide a feasible route to essentially increase this efficiency limit.

As a comparison, although a double-side deposited absorber and emitter used in planar STPV system can also be directly employed in the cage-type system, its absorber part is inert during the emission process which will decrease the system efficiency distinctly.

The HAE can work not only in STPV systems but also in fuel thermophotovoltaics (TPV) systems, which possesses the inherent capability of convenient heat storage compared to solar photovoltaic technologies. The unique priority of the one-side bifunctional structure makes the other side of our HAE ideal for the integration of STPV and TPV systems. As illustrated in Figure 4e, a fuel tunnel can then be directly attached to the heat fluid side so that an all-climate STPV system is possible. During sunny days, the HAE absorbs concentrated sunlight and radiates the desired narrowband thermal emission

to the surrounding PV cells. In the meanwhile, the extra heat can be stored by the underlying energy storage materials; when sunlight is not available, the heat fluid in the tunnel provides thermal energy to HAE, driving the TPV system operation. The HAE-based all-climate STPV-TPV system can provide a competitive power supply solution to the non-ideal environments and emergency situations such as peak load of grid, etc.

In conclusion, we experimentally demonstrated a bifunctional HAE for STPV by integrating efficient solar absorber and perfect infrared emitter on one surface. The CPA-based infrared absorptivity makes our HAE an ideal choice for selective narrowband thermal emission in STPV system, with multiple advantages of perfect, angle-independent, and high-temperature stable infrared thermal emissivity. By further tuning thickness of the top HfO₂ layer, the perfect thermal emitter can serve as an efficient broadband solar absorber simultaneously. The pronounced optical performance (measured thermal emissivity of $\approx 97\%$, average solar absorptivity of $\approx 80\%$), combined with the scalable, lithography-free physical deposition processes, makes our HAE a promising candidate for unique STPV systems such as the radiation-depressed cage-type STPV, shedding light on the integrated all-climate STPV-TPV systems in future.

Supporting Information

Supporting Information is available from the Wiley Online Library or from the author.

Acknowledgements

The authors acknowledge the microfabrication center of National Laboratory of Solid State Microstructures (NLSSM) for technique support. This work was jointly supported by the National Key Research and Development Program of China (No. 2017YFA0205700), the State Key Program for Basic Research of China (No. 2015CB659300), the National Natural Science Foundation of China (Nos. 61735008, 11874211, 11621091, 11574143, 21805132), Natural Science Foundation and Qing Lan project of Jiangsu Province (Nos. BK20180341, BK20151382), and the Fundamental Research Funds for the Central Universities (Nos. 021314380135, 021314380128).

Conflict of Interest

The authors declare no conflict of interest.

Keywords

coherence-enhanced absorption, hybrid absorber–emitter, thermophotovoltaics

Received: June 24, 2018

Revised: October 5, 2018

Published online: October 23, 2018

- [1] D. M. Bierman, A. Lenert, W. R. Chan, B. Bhatia, I. Celanovic, M. Soljačić, E. N. Wang, *Nat. Energy* **2016**, 1, 16068.
- [2] A. Kohiyama, M. Shimizu, H. Yugami, *Appl. Phys. Express* **2016**, 9, 112302.

- [3] M. Shimizu, A. Kohiyama, H. Yugami, *J. Photonics Energy* **2015**, 5, 053099.
- [4] A. P. Raman, M. A. Anoma, L. Zhu, E. Rephaeli, S. Fan, *Nature* **2014**, 515, 540.
- [5] Y. Zhai, Y. Ma, S. N. David, D. Zhao, R. Lou, G. Tan, R. Yang, X. Yin, *Science* **2017**, 355, 1062.
- [6] H. Ghasemi, G. Ni, A. M. Marconnet, J. Loomis, S. Yerci, N. Miljkovic, G. Chen, *Nat. Commun.* **2014**, 5, 4449.
- [7] L. Zhou, Y. L. Tan, J. Y. Wang, W. C. Xu, Y. Yuan, W. S. Cai, S. N. Zhu, J. Zhu, *Nat. Photonics* **2016**, 10, 393.
- [8] C. Jia, Y. J. Li, Z. Yang, G. Chen, Y. G. Yao, F. Jiang, Y. D. Kuang, G. Pastel, H. Xie, B. Yang, S. Das, L. B. Hu, *Joule* **2017**, 1, 588.
- [9] E. Sakr, P. Bermel, *Opt. Express* **2017**, 25, A880.
- [10] J. Moon, D. Lu, B. VanSaders, T. K. Kim, S. D. Kong, S. H. Jin, R. K. Chen, Z. W. Liu, *Nano Energy* **2014**, 8, 238.
- [11] Y. Wang, L. Zhou, Q. H. Zheng, H. Lu, Q. Q. Gan, Z. F. Yu, J. Zhu, *Appl. Phys. Lett.* **2017**, 110, 201108.
- [12] H. Tian, Z. G. Zhou, T. R. Liu, C. Karina, U. Guler, V. Shalae, P. Bermel, *Appl. Phys. Lett.* **2017**, 110, 141101.
- [13] J. N. Winn, Y. Fink, S. Fan, J. Joannopoulos, *Opt. Lett.* **1998**, 23, 1573.
- [14] F. O'Sullivan, I. Celanovic, N. Jovanovic, J. Kassakian, S. Akiyama, K. Wada, *J. Appl. Phys.* **2005**, 97, 033529.
- [15] J. Zhou, X. Chen, L. J. Guo, *Adv. Mater.* **2016**, 28, 3017.
- [16] P. N. Dyachenko, S. Molesky, A. Y. Petrov, M. Stormer, T. Krekeler, S. Lang, M. Ritter, Z. Jacob, M. Eich, *Nat. Commun.* **2016**, 7, 11809.
- [17] J. H. Kim, S. M. Jung, M. W. Shin, *Opt. Mater.* **2017**, 72, 45.
- [18] F. Cao, D. Kraemer, T. Sun, Y. Lan, G. Chen, Z. Ren, *Adv. Energy Mater.* **2015**, 5, 1401042.
- [19] B. Liu, W. Gong, B. Yu, P. Li, S. Shen, *Nano Lett.* **2017**, 17, 666.
- [20] S. Molesky, C. J. Dewalt, Z. Jacob, *Opt. Express* **2013**, 21, A96.
- [21] J. Y. Lu, A. Raza, S. Noorulla, A. S. Alketbi, N. X. Fang, G. Chen, T. J. Zhang, *Adv. Opt. Mater.* **2017**, 5, 1700222.
- [22] A. Naldoni, U. Guler, Z. X. Wang, M. Marelli, F. Malara, X. G. Meng, L. V. Besteiro, A. O. Govorov, A. V. Kildishev, A. Boltasseva, V. M. Shalae, *Adv. Opt. Mater.* **2017**, 5, 1601031.
- [23] Y. R. Qu, Q. Li, K. K. Du, L. Cai, J. Lu, M. Qiu, *Laser Photonics Rev.* **2017**, 11, 1700091.
- [24] W. Li, U. Guler, N. Kinsey, G. V. Naik, A. Boltasseva, J. G. Guan, V. M. Shalae, A. V. Kildishev, *Adv. Mater.* **2014**, 26, 7959.
- [25] M. Chirumamilla, A. Chirumamilla, Y. Q. Yang, A. S. Roberts, P. K. Kristensen, K. Chaudhuri, A. Boltasseva, D. S. Sutherland, S. I. Bozhevolnyi, K. Pedersen, *Adv. Opt. Mater.* **2017**, 5, 1115.
- [26] S. Han, J. H. Shin, P. H. Jung, H. Lee, B. J. Lee, *Adv. Opt. Mater.* **2016**, 4, 1265.
- [27] E. Rephaeli, S. Fan, *Opt. Express* **2009**, 17, 15145.
- [28] P. Li, B. Liu, Y. Ni, K. K. Liew, J. Sze, S. Chen, S. Shen, *Adv. Mater.* **2015**, 27, 4585.
- [29] M. Garín, D. Hernández, T. Trifonov, R. Alcubilla, *Sol. Energy Mater. Sol. Cells* **2015**, 134, 22.
- [30] V. Rinnerbauer, A. Lenert, D. M. Bierman, Y. X. Yeng, W. R. Chan, R. D. Geil, J. J. Senkevich, J. D. Joannopoulos, E. N. Wang, M. Soljačić, I. Celanovic, *Adv. Energy Mater.* **2014**, 4, 1400334.
- [31] J. B. Chou, Y. X. Yeng, Y. E. Lee, A. Lenert, V. Rinnerbauer, I. Celanovic, M. Soljatic, N. X. Fang, E. N. Wang, S. G. Kim, *Adv. Mater.* **2014**, 26, 8041.
- [32] C. Wu, B. Neuner III, J. John, A. Milder, B. Zollars, S. Savoy, G. Shvets, *J. Opt.* **2012**, 14, 024005.
- [33] H. Wang, Q. Chen, L. Wen, S. Song, X. Hu, G. Xu, *Photonics Res.* **2015**, 3, 329.
- [34] S. Behera, J. Joseph, *J. Appl. Phys.* **2017**, 122, 193104.
- [35] Y. D. Chong, L. Ge, H. Cao, A. D. Stone, *Phys. Rev. Lett.* **2010**, 105, 053901.

- [36] W. Wan, Y. Chong, L. Ge, H. Noh, A. D. Stone, H. Cao, *Science* **2011**, 331, 889.
- [37] M. Pu, Q. Feng, M. Wang, C. Hu, C. Huang, X. Ma, Z. Zhao, C. Wang, X. Luo, *Opt. Express* **2012**, 20, 2246.
- [38] J. Luo, S. Li, B. Hou, Y. Lai, *Phys. Rev. B* **2014**, 90, 165128.
- [39] S. Li, J. Luo, S. Anwar, S. Li, W. Lu, Z. H. Hang, Y. Lai, B. Hou, M. Shen, C. Wang, *Sci. Rep.* **2015**, 4, 7369.
- [40] H. Deng, Z. Li, L. Stan, D. Rosenmann, D. Czaplewski, J. Gao, X. Yang, *Opt. Lett.* **2015**, 40, 2592.
- [41] G. Nimtz, U. Panten, *Ann. Phys. (Berlin)* **2010**, 19, 53.
- [42] M. Shimizu, A. Kohiyama, H. Yugami, *J. Quant. Spectrosc. Radiat. Transfer* **2018**, 212, 45.
- [43] M. Chirumamilla, A. S. Roberts, F. Ding, D. Y. Wang, P. K. Kristensen, S. I. Bozhevolnyi, K. Pedersen, *Opt. Mater. Express* **2016**, 6, 2704.
- [44] E. Blandre, M. Shimizu, A. Kohiyama, H. Yugami, P. O. Chapuis, R. Vaillon, *Opt. Express* **2018**, 26, 4346.
- [45] A. S. Roberts, M. Chirumamilla, K. Thilsing-Hansen, K. Pedersen, S. I. Bozhevolnyi, *Opt. Express* **2015**, 23, A1111.
- [46] R. N. Patil, E. C. Subbarao, *J. Appl. Crystallogr.* **1969**, 2, 281.
- [47] F. C. Nix, D. MacNair, *Phys. Rev.* **1942**, 61, 74.
- [48] A. Lenert, D. M. Bierman, Y. Nam, W. R. Chan, I. Celanović, M. Soljačić, E. N. Wang, *Nat. Nanotechnol.* **2014**, 9, 126.
- [49] A. Leroy, B. Bhatia, L. Zhao, E. N. Wang, *Opt. Express* **2018**, 26, A462.